Computational Materials Science 135 (2017) 29–42

Contents lists available at ScienceDirect

Computational Materials Science

journal homepage: www.elsevier.com/locate/commatsci

Piezoelectric and elastic properties of multiwall boron-nitride nanotubes and their fibers: A molecular dynamics study

Vesselin Yamakov [a,*], Cheol Park [b], Jin Ho Kang [a], Xiaoming Chen [c], Changhong Ke [c], Catharine Fay [b]

[a] National Institute of Aerospace, Hampton, VA 23666, USA
[b] NASA Langley Research Center, Hampton, VA 23681, USA
[c] Department of Mechanical Engineering, State University of New York at Binghamton, Binghamton, NY 13902, USA

ARTICLE INFO

Article history:
Received 14 December 2016
Received in revised form 15 March 2017
Accepted 30 March 2017

Keywords:
Boron nitride nanotube
Stiffness
Piezoelectricity
Molecular dynamics

ABSTRACT

Piezoelectric and elastic properties of multiwall boron-nitride nanotubes are studied using a classical molecular dynamics model with an incorporated strain-dependent dipole potential energy term. The results are applied to predict the piezoelectric and elastic properties of a boron-nitride nanotubes fiber with experimentally obtained diameter and wall number distribution of the nanotubes synthesized by high-temperature pressure methods. Nanotubes of $(m, 0)$-type (zig-zag nanotubes) of up to 10 wall layers and up to 7 nm in diameter are simulated in tension along the tube axis. While the tensile stiffness of all of the simulated nanotubes increases linearly with their radius and the number of wall layers, a substantial difference in the piezoelectric response is found between nanotubes of even and odd number of wall layers due to the particular stacking sequence of the boron-nitride layers. The piezoelectric polarization per unit length of odd-layer boron-nitride nanotubes *increases* linearly with the tube radius, but *decreases* with the number of layers. By contrast, the piezoelectric polarization of even-layer nanotubes is *independent* of the radius, but *increases* linearly with the number of layers. Analytical expressions for the multiwall boron-nitride nanotubes stiffness and piezoelectric coefficients are provided for use in continuum mechanics finite-element models.

1. Introduction

One attractive feature of boron nitride nanotubes (BNNTs) [1,2], which differentiates them from their pure carbon structural counterpart, carbon nanotubes (CNTs), is their intrinsic piezoelectricity [3–7]. This is due to the partially ionic characteristic of the boron (B)–nitrogen (N) bond, compared to the purely covalent C—C bond in CNTs. BNNTs were also shown to possess strong electrostrictive [8] and flexoelectric [9] properties. In combination with their high mechanical modulus and strength matching those of CNT [10–19], superior high-temperature oxidation resistance [2], and enhanced radiation shielding against neutrons [8,9,20], BNNTs are very attractive materials for multifunctional applications in extreme environments.

Analytical and simulation studies of the piezoelectric behavior of BNNTs have been mostly focused on single-wall BNNTs (SW-BNNTs) [3–7,21–24], while synthesized BNNTs are predominantly multi-wall BNNTs (MW-BNNTs)[1] [1,8,25]. A comparison between single- and double-wall BNNTs was performed in a series of molecular dynamics (MD) simulations to study their vibrational behavior [26,27], and their structural stability [28]. It is argued [1] that the partially ionic characteristic of the B—N bond in the hexagonal boron nitride (hBN) structure of BNNT tends to stabilize the formation of double-wall (DW-) and MW-BNNTs by favoring an alternating B-over-N and N-over-B placement of atoms between two adjacent hBN layers (known as AA′-stacking) [29,30]. The alternate stacking of the hBN layers reverses the dipole direction in each consecutive layer. As a result, as noted in a recent MD study [31], consecutive hBN layers polarize in opposite directions and partially cancel each other to decrease the overall piezoelectric effect in MW-BNNTs. This cancellation effect is more pronounced in BNNTs with even number of layers than with odd number of layers, and is a very interesting feature unique only for MW-BNNTs.

The goal of this work is to investigate in detail the elastic and piezoelectric properties of MW-BNNTs utilizing a recently

* Corresponding author.
E-mail address: yamakov@nianet.org (V. Yamakov).

[1] In addition to SW-, DW-, and MW-BNNT for a single-, double-, and multi-wall BNNT, the general abbreviation LW-BNNTs will be used throughout the paper, where L = 1, 2, 3, ... indicates the number of layers in the BNNT wall.

http://dx.doi.org/10.1016/j.commatsci.2017.03.050
0927-0256/

proposed method [21] for incorporating piezoelectric behavior into an empirical interatomic potential of Tersoff type for modeling hBN structures by MD simulations. The method was shown to accurately represent the piezoelectric properties of SW-BNNTs as calculated by first-principle calculations [4]. At the same time, the much lower computational cost of the MD technique allows the simulation of large structures, such as MW-BNNTs containing several tens of thousands of atoms. MW-BNNTs of (m, 0)-crystallographic indices [32] (zig-zag nanotubes) are chosen for this study. The (m, 0)-type nanotubes exhibit piezoelectric polarization along their axis when stretched, which is the simplest mode of deformation to simulate, and provides the most accurate results. Analytical representation of the simulation results is also given, based on the analytical expressions for the tensile stiffness of MW-BNNTs, derived by Song et al. [33], and on the extension of the piezoelectric model for SW-BNNTs presented earlier [21]. This analytical representation allows the prediction of the piezoelectric behavior of MW-BNNTs of arbitrary number of layers and of any given radius. While the study is focused on the zig-zag type of nanotubes, which exhibits highest piezoelectric polarization along their axis when stretched among all chiral types [4], the results can be extended in a straightforward way to include BNNTs of general chirality.

The analytical expressions derived from the MD model were applied to predict the stiffness and the piezoelectric coefficients of a fiber consisting of 1000 BNNTs with experimentally obtained diameter and wall number distribution. The BNNTs were synthesized by high-temperature pressure (HTP) methods [25,34] and their structural characterization was performed using high resolution transmission electron microscopy (HRTEM) in combination with atomic force microscopy (AFM).

This paper is constructed as follows. The simulation model for a piezoelectric MW-BNNT is described in Section 2. Section 3 presents the results, first, for the elastic properties of MW-BNNTs, and then for the direct and converse piezoelectric effect in MW-BNNTs. The properties of individual BNNT fibers are considered in Section 4. A conclusion is given in Section 5.

2. Molecular dynamics model for piezoelectric multi-wall BNNTs

2.1. Piezoelectric energy upgrade of the Tersoff potential for a hexagonal BN layer structure

The empirical atomistic piezoelectric model for reproducing the elasto-mechanical properties of hBN layer structures in this study implements a Tersoff type of interatomic potential parameterized by Sevik et al. [35]. The potential is targeted to reproduce closely the structural, mechanical, and vibrational properties of hBN by fitting to first-principle *ab initio* calculations [35]. The thermomechanical properties of this potential are studied in detail by Singh et al. [36].

The piezoelectric behavior of the hBN lattice is simulated [21] by introducing a dipole moment, p_{BN}, to each individual B—N bond. The electrostatic potential created by the dipole moment is added to the Tersoff potential. The direction of the dipole vector follows the direction of the B—N bond polarity (from N to B), and the dipole magnitude is defined as [21]

$$p_{BN} = p_0\left[\frac{r_{BN}-r_0}{r_0} + t_\theta\sum_{i=1}^{4}\left(\frac{1}{2}+\cos\theta_i\right)\right], \tag{1}$$

where p_0 and t_θ are fitting parameters, r_{BN} and r_0 are the current and the equilibrium length of the B—N bond, and $\theta_{i=1\ldots4}$ are the bond angles between the B—N bond and the four neighboring bonds in the hBN arrangement. The suggested constitutive relation in Eq. (1) consists of two terms that counteract each other to produce a polarization proportional to the deviation of the crystal lattice from the hexagonal symmetry. The rationale behind this form comes from theoretical [3] and *ab initio* [5] studies, which explains the piezoelectric effect in BNNTs as a counteraction between electronic and ionic spontaneous polarizations that cancel exactly unless the symmetry of the hBN lattice is broken by inter-tube interactions or elastic distortions. It was shown [21] that Eq. (1) leads to a piezoelectric tensor that satisfies the $3m$ symmetry of the hBN lattice with coefficients expressed as

$$e_{xxx} = -e_{xyy} = -e_{yxy} = -e_{yyx} = \frac{p_0}{2\sqrt{3}r_0^2}[(1+A) - 3t_\theta(1-A)] \tag{2}$$

where the values of r_0 and A are defined through the interatomic potential and its first and second spatial derivatives at equilibrium [33]. The constant A relates to the magnitude of a shift vector, δ, between the B and N sub-lattices of an hBN plane under strain ε, which was introduced in Ref. [33] and expressed as

$$\delta_\lambda = \frac{2}{3}A\varepsilon_{\alpha\beta}\sum_{i=1}^{3} n_\alpha^{(i)} n_\beta^{(i)} n_\lambda^{(i)}, \tag{3}$$

where the summation is over the three neighboring (i) atoms of bond directions $\boldsymbol{n}^{(i)}$. The subscripts, α, β, and λ, express the Cartesian components of the vector quantities in Eq. (3).

Using Eq. (2) [21], the piezoelectric coefficients per unit cell area can be expressed in electron charges per nanometer (e/nm) if p_0 is in (e × nm), and r_0 is in units of nm. To convert to the standard piezoelectric coefficients per unit volume, one has to divide Eq. (2) by the interlayer spacing h.

The tube polarization per unit cell is given as

$$p_{cell} = e_{11}\varepsilon_s + e_{14}\varepsilon_t \tag{4a}$$

where ε_s and ε_t are the strain in stretch along, and in torsion around the tube axis, respectively. The coefficients, e_{11} and e_{14}, are the nanotube piezoelectric coefficients in stretch and torsion, respectively, and are related to the hBN coefficients in Eq. (2), and to the chiral angle, φ, as

$$\begin{vmatrix} e_{11} = e_{xxx}(1+\nu)\cos 3\varphi \\ e_{14} = e_{yxy}\sin 3\varphi \end{vmatrix}. \tag{4b}$$

Eq. (2) can be used to adjust the fitting parameters p_0 and t_θ to reproduce the piezoelectric constants of a flat hBN sheet as calculated from first-principles for any given 3-body interatomic potential (not necessarily of Tersoff type). Eq. (2) alone is not enough to define both of the fitting parameters. Additional condition for their determination is to reproduce the increase of the piezoelectric coefficient of a SW-BNNT with the decrease of the nanotube radius due to curvature effects, as calculated from first principles [4]. A fitting method such as the least-square fit, could be used for this purpose. The fit, together with the values of r_0 and A in Eq. (2), depends on the choice of the interatomic potential for a neutral BNNT. In Ref. [21], p_0 and t_θ were given for the case of two previously reported and widely used potentials: by Albe et al. [37], and by Sekkal et al. [38]. The fitted values of p_0 and t_θ for the Sevik et al. potential [35] used in this work are presented in Table 1, together with r_0, A, Poisson's ratio, ν, and the Young's modulus, Y. The fit reproduces the e_{xxx} coefficient in Eq. (2) as calculated by Sai and Mele [4].

2.2. Lennard-Jones potential for inter-wall interactions

An essential part of the MW-BNNT model is the interwall interaction between the nanotube layers. This work uses a Lennard-Jones (L-J) type of potential to model this interaction, where the potential energy $U_{\alpha\beta}(r)$ between two atoms of chemical type α or

Table 1
Results for the fitting parameters p_0 and t_θ to reproduce the e_{xxx} coefficient in Eq. (2) as calculated in [4], together with the values of r_0, A, B, ν, and the Young modulus, Y, calculated for the applied Tersoff interatomic potential [35].

r_0 (nm)	A	B (eV/nm^2)	ν	Y (TPa)	p_0 (e × nm)	t_θ	e_{xxx} (2)
0.1442	−0.672	16,507	0.311	0.750	−0.054	0.5	1.63 (e/nm) 0.086 (e/Bohr) [4]

β (α, β ≡ B, N) is defined as a function of the distance r between the atoms as

$$U_{\alpha\beta}(r) = C_{12}^{\alpha\beta} r^{-12} - C_6^{\alpha\beta} r^{-6}, \quad (\alpha, \beta = B, N) \tag{5}$$

The constants, $C_{12}^{\alpha\beta}$ and $C_6^{\alpha\beta}$, express the strength of the nuclear repulsion and the van der Waals attraction, respectively. Their values, given in Table 2, are chosen so that $U_{\alpha\beta}(r)$ reproduces closely the potential energy of a crystalline hBN (a periodically repeating hBN layered structure), and of a bilayer hBN as obtained through density functional theory (DFT) calculations [29] (Fig. 1). The values of the $C_6^{\alpha\beta}$ term were initially taken from the van der Waals C_6 coefficients calculated by Hod [30], which ensured close reproduction of the van der Waals attraction, and the overall potential curve, if the repulsive part is also reproduced correctly. Unfortunately, it was found that the r^{-12} dependence in the L-J potential was too steep to reproduce correctly the Pauli repulsion. To preserve the attractive part of the interaction and to reproduce the entire range of the potential energy curve, $C_6^{\alpha\beta}$ had to be modified in combination with $C_{12}^{\alpha\beta}$. The resulting equilibrium interplanar spacing h_0 at $T = 0$ K for the L-J potential in Eq. (5), is equal to 0.333 nm for a bilayer, and 0.330 nm for a bulk hBN, which is within the reported values between 0.33 and 0.34 nm [29,30].

Significant attention has been given to the ability of the L-J potential to reproduce the energies of the AA', AB_1, and AB_2 stacking modes closely to those reported by Marom et al. [29] (Table 3). These three modes have the common feature that the stacking layers are flipped at 180° with respect to each other and are exactly overlapping, or shifted by plus or minus one bond length along one of the B—N bond directions as given in the insets in Table 3. The AA' mode has the lowest potential energy and is the optimal stacking mode, which is well reproduced by the L-J potential. The non-trivial difference between the energies of the otherwise similar AB_1 (B-B atoms overlap) and AB_2 (N-N atoms overlap) modes found through *ab initio* calculations [30] is also well reproduced. This energy difference is due to the stronger Pauli repulsion between N atoms than between B atoms.

Table 3 also gives the L-J energies of the *AA* and *AB* modes. The *AA* mode is formed from two identical hBN layers overlapping exactly with each other. The *AB* mode is formed by a relative shift of one bond length of the layers along one of the B—N bond directions (see insets in Table 3). The *AB* mode is the optimal stacking mode of graphite, and has also been reported to form in thin sheets of hBN material composed of just a few layers [39]. The *AA* and *AB* modes were not used in the fitting procedure of the L-J potential and are not relevant to the simulations in this study, but are given here for completeness. The *AA* mode, where both B—B and N—N overlap, is expected to have the highest energy of all stacking modes, while being close to the AB_2 mode due to the dominant role of the Pauli repulsion at the N—N overlap. The energy of the *AB* mode is only slightly higher (by 0.5 meV) than the energy of the AA' mode, which suggests that the *AB* mode might exist in a multilayer hBN system. In fact, *AB* stacking has been observed to form around the edges of a layered hBN structure during sonication [39].

Table 2
Coefficients for the Lennard-Jones potential in Eq. (5) for interwall interactions between B—B, N—N, and B—N pairs of atoms in a MW-BNNT.

Coeff.	α-β		
	B—B	N—N	B—N
$C_{12}^{\alpha\beta}$ (eV × nm^{12})	2.757E−8	1.779E−7	−1.044E−8
$C_6^{\alpha\beta}$ (eV × nm^6)	5.171E−5	1.478E−5	2.612E−5

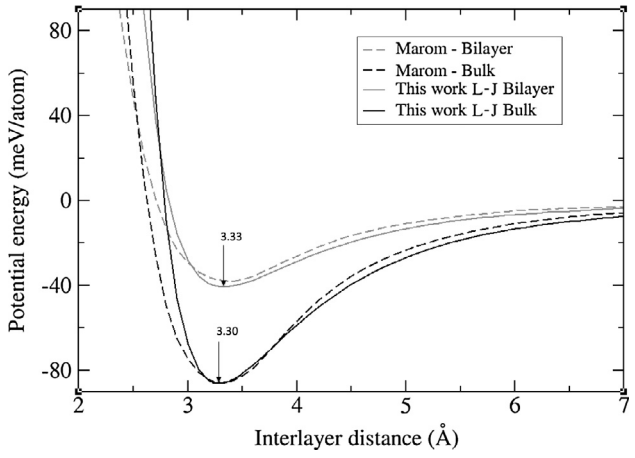

Fig. 1. Inter-layer potential energy expressed through the Lennard-Jones (L-J) potential Eq. (5) and compared to density functional theory calculations by Marom et al. [29].

2.3. Simulation model and nanotube configurations

Simulations were carried out on a series of SW-BNNTs and MW-BNNTs. All BNNTs were of equal length, $H = 5.19$ nm, and were simulated under periodic boundary conditions imposed along the tube axis, set as the x-axis. Free boundary conditions were imposed on the perpendicular y- and z-directions. After equilibration at $T = 10$ K, a tensile strain was applied homogeneously along the x-axis, to prevent the initiation of shock waves. The stretching was applied in 8 increments of 0.25% each, giving a total strain of $\varepsilon_{xx} = 2\%$, which is small enough for non-linear effects to be negligible. After each increment, the tubes were equilibrated for 35 ps, or 100,000 MD steps, during which time measurements were taken periodically at each 100 MD steps, and the results of the last 500 measurements, during which the system is assumed to have achieved equilibrium, were averaged to give the final measurement.

All chosen BNNTs in the simulations were of (m, 0)-type (zig-zag nanotubes) with m being in the range from 5 to 86 (not all values were simulated), giving tubes of radius [32]

$$R_{(m,0)} = m(\sqrt{3} r_0 / 2\pi) \tag{6}$$

ranging from $R_{(5,0)} = 0.2$ nm to $R_{(86,0)} = 3.4$ nm. Only SW-BNNTs of $m = 5$, 6, 7, 8, 9, and 10 were simulated, since SW-BNNTs with $m > 10$ tend to wobble and could not keep a perfect cylindrical form.

Limiting the study to zig-zag nanotubes only does not limit the applicability of the presented methodology to BNNT systems of different chirality. The effect of chirality on the mechanical properties of BNNTs is not pronounced and is difficult to be assessed experi-

Table 3
Stacking layer energies E_{LJ} for a bilayer hBN, as obtained from the Lennard-Jones potential in Eq. (5). The insets indicate the corresponding stacking arrangement of the B (green), and N (blue) atoms of the two adjacent layers.

Energy (meV/atom)	Type				
	AA′	AB_1	AB_2	*AA*	*AB*
E_{LJ}	−40.6	−39.2	−34.6	−34.2	−40.1
ΔE this work	0	1.4	6.0	6.4	0.5
ΔE *ab initio*[a]	0	0.875–2.0	6.5 – 12.0	–	–

[a] Ref. [29,30] and the references therein.

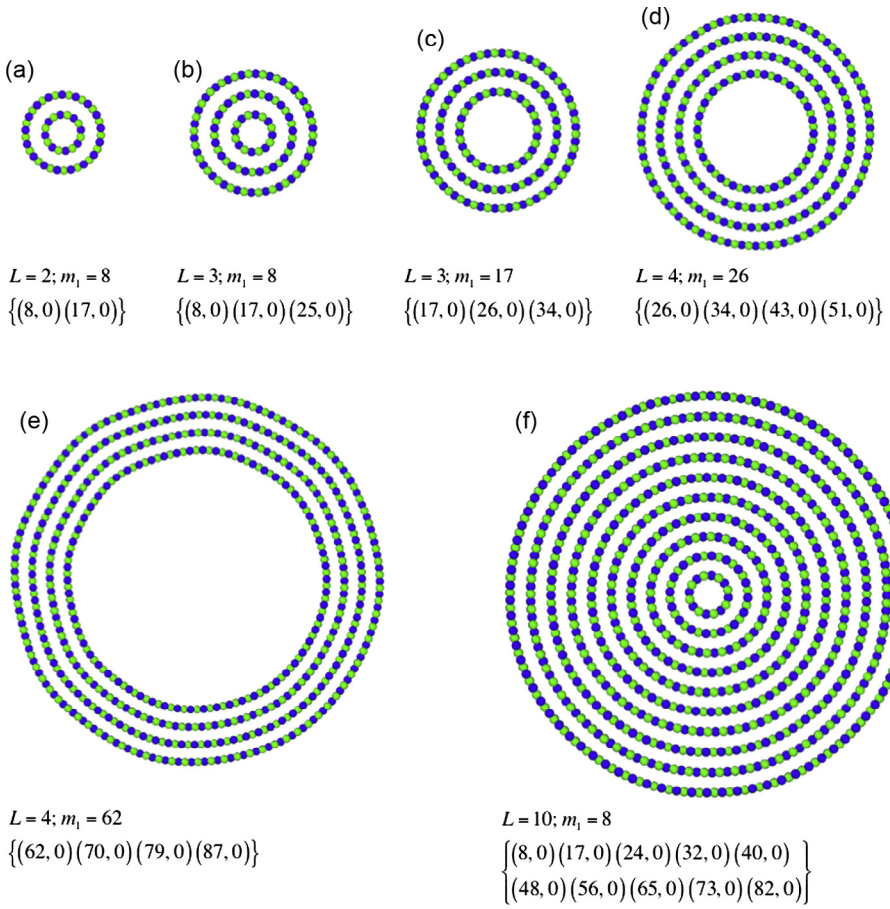

Fig. 2. Cross-sectional snapshots of several of the simulated multi-wall BNNTs depicting their layered wall atomic structure which consists of boron (green) and nitrogen (blue) atoms. (For interpretation of the references to colour in this figure legend, the reader is referred to the web version of this article.)

mentally. *Ab initio* computations [40] have shown that the elastic constants of zig-zag (chiral angle, $\varphi = 0°$) and of armchair or (*m*, *m*)-type (chiral angle, $\varphi = 30°$) differ slightly (~1%) only for the thinnest nanotubes (R < 0.3 nm). The Poison ratio for the zig-zag BNNTs converges slower to the isotropic planar value, remaining systematically higher compared to armchair BNNTs. More recent study by Peng et al. [41] is in agreement with these findings.

Chirality has a significant effect on the piezoelectric properties, but this effect is well understood and can be predicted from the results for zig-zag BNNTs using the cosine dependence with the chiral angle, φ, as expressed through Eqs. (4a) and (4b). A significant difference from zig-zag BNNTs is that armchair BNNTs polarize in torsion, instead of in stretch, as Eq. (4b) predicts for $\varphi = 30°$. MD simulation studies on deformation of armchair BNNTs in torsion were reported by Ansari and Ajori [23,24]. Similar torsion deformation models can be used to study piezoelectric effects in armchair MW-BNNTs.

MW-BNNTs of *L*-wall layers were built as a system of *L* concentric SW-BNNTs of indices $(m_l, 0)$ (the subscript, $l = 1, 2, \ldots, L$, indicates the layer number) placed inside each other in *AA′* stacking sequence. The resultant MW-BNNTs are indexed as $\{(m_1, 0)\ldots(m_L, 0)\}$ with $L = 2, 3, \ldots 10$. Several examples are given in Fig. 2. The indices m_l follow the iterative rule, $m_{l+1} = m_l + \Delta m_l$; $(l = 1, 2, \ldots L-1)$. The first m_1, and the last m_L numbers define the inner R_1, and the outer R_L radius of the nanotube (see Eq. (6), and Fig. 3). The overall radius of the nanotube R is defined as the outer radius, $R = R_L$. The values of the increments, Δm_l, were chosen to minimize the overall potential energy of a MW-BNNT of a given *L*. Geometrically, using Eq. (6), the interlayer distance between two adjacent layers is

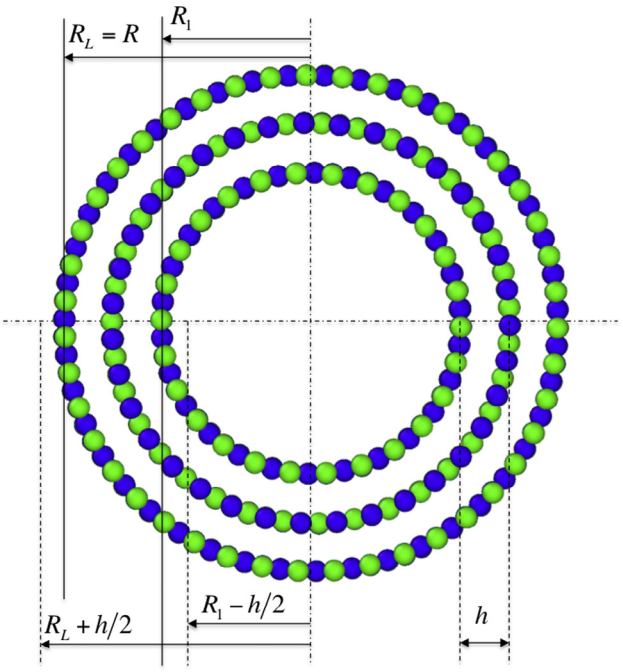

Fig. 3. Cross-section snapshot of a three wall BNNT of indices {(26, 0) (35, 0) (43, 0)} defining the inner R_1, and the outer R_L, nanotube radii, together with the interlayer distance h. Boron atoms are shown in green, and nitrogen atoms are shown in blue. (For interpretation of the references to colour in this figure legend, the reader is referred to the web version of this article.)

$$h_l(\Delta m_l) = \Delta m_l(\sqrt{3}r_0/2\pi); \quad \Delta m_l = m_{l+1} - m_l; \quad (l = 1, 2, \ldots L-1). \tag{7}$$

The two closest h_l to the equilibrium hBN interplanar distance of $h_0 = 0.333$ nm are obtained for $\Delta m_l = 8$ and 9, equal to $h_l = 0.318$ nm, and $h_l = 0.358$ nm, respectively. Thus, Δm_l for each l is varied to be either 8 or 9, producing 2^{L-1} different nanotubes for each given L and m_1. After equilibration at T = 10 K, the nanotube with the lowest potential energy is selected and used for this study. All of the selected nanotubes are listed in Table 4, including the five simulated as isolated SW-BNNTs ($L = 1$). It was found that the lowest energy configuration for DW-BNNTs ($L = 2$) is always obtained when $\Delta m_1 = 9$, while Δm_l for higher order MW-BNNTs ($L > 2$) varies between 8 and 9. Several of the nanotube configurations selected for simulation are shown in Fig. 2, including the smallest (Fig. 2(a)) and the largest (Fig. 2(f)) configurations. An interesting observation is that nanotubes of large radius but low number of layers, such as the one in Fig. 2e, tend to form a faceted cross-section of an equilateral polygon, rather than circular. The reason is that the polygon configuration minimizes the curvature induced strain energy of the nanotube layers, while seeking a balance with the increased bond bending energy localized at the kinks. In addition, the polygon shaped layers can better follow the lowest energy AA' stacking sequence than the more circular layers, which, due to their different radii, cannot maintain the AA' stacking everywhere. The result is consistent with prior findings that BNNTs of larger tube diameters and smaller number of walls are more simple structures in their transverse directions [42,43]. It is noted that the polygon effect is likely more pro-

Table 4
Simulated configurations of multi-wall BNNTs from $L = 1$ to 10 layers given as {(m_1, 0) (m_2, 0) ...}, and as {Δm_1, Δm_2, ...} for $L > 1$, where $\Delta m_l = m_{l+1} - m_l$, with ($l = 1, 2, \ldots L-1$) from Eq. (7).

L	{(m_1, 0) (m_2, 0) ...}	{Δm_1, Δm_2, ...}
1	{(5, 0)}; {(6, 0)}; {(7, 0)}; {(8, 0)}; {(9, 0)}	–
2	{(8, 0) (17, 0)}; {(9, 0) (18, 0)}; {(10, 0) (19, 0)}; {(11, 0) (20, 0)}	All {$\Delta m_1 = 9$}
	{(12, 0) (21, 0)}; {(13, 0) (22, 0)}; {(14, 0) (23, 0)}; {(15, 0) (24, 0)}	
	{(16, 0) (25, 0)}; {(17, 0) (26, 0)}; {(18, 0) (27, 0)}; {(19, 0) (28, 0)}	
	{(20, 0) (29, 0)}; {(21, 0) (30, 0)}; {(22, 0) (31, 0)}; {(23, 0) (32, 0)}	
	{(24, 0) (33, 0)}; {(25, 0) (34, 0)}; {(26, 0) (35, 0)}; {(34, 0) (43, 0)}	
	{(51, 0) (60, 0)}; {(60, 0) (69, 0)}; {(68, 0) (77, 0)}; {(77, 0) (86, 0)}	
3	{(8, 0) (17, 0) (25, 0); {(17, 0) (26, 0) (34, 0)}; {(26, 0) (35, 0) (43, 0)}	{9, 8}; {9, 8}; {9, 8}
	{(35, 0) (44, 0) (52, 0)}; {(44, 0) (53, 0) (61, 0)}; {(53, 0) (62, 0) (70, 0)}	{9, 8}; {9, 8}; {9, 8}
	{(62, 0) (71, 0) (79, 0)}; {(71, 0) (80, 0) (88, 0)}	{9, 8}; {9, 8}
4	{(8, 0) (17, 0) (26, 0) (34, 0)}; {(17, 0) (26, 0) (34, 0) (43, 0)}	{9, 9, 8}; {9, 8, 9}
	{(26, 0) (34, 0) (43, 0) (51, 0)}; {(35, 0) (43, 0) (52, 0) (60, 0)}	{8, 9, 8}; {8, 9, 8}
	{(44, 0) (52, 0) (61, 0) (70, 0)}; {(53, 0) (61, 0) (70, 0) (78, 0)}	{8, 9, 9}; {8, 9, 8}
	{(62, 0) (70, 0) (79, 0) (87, 0)}	{8, 9, 9}
5	{(8, 0) (17, 0) (26, 0) (34, 0) (43, 0)}; {(17, 0) (25, 0) (33, 0) (42, 0) (50, 0)}	{9, 9, 8, 9}; {8, 8, 9, 8}
	{(26, 0) (34, 0) (42, 0) (51, 0) (59, 0)}; {(35, 0) (43, 0) (51, 0) (60, 0) (68, 0)}	{8, 8, 9, 8}; {8, 8, 9, 8}
	{(44, 0) (52, 0) (60, 0) (69, 0) (77, 0)}; {(53, 0) (61, 0) (69, 0) (78, 0) (86, 0)}	{8, 8, 9, 8}; {8, 8, 9, 8}
6	{(8, 0) (17, 0) (26, 0) (35, 0) (43, 0) (52, 0)}	{9, 9, 9, 8, 9}
	{(17, 0) (25, 0) (33, 0) (42, 0) (50, 0) (59, 0)}	{8, 8, 9, 8, 9}
	{(26, 0) (34, 0) (42, 0) (51, 0) (59, 0) (68, 0)}	{8, 8, 9, 8, 9}
	{(35, 0) (43, 0) (51, 0) (60, 0) (68, 0) (77, 0)}	{8, 8, 9, 8, 9}
	{(44, 0) (52, 0) (60, 0) (69, 0) (77, 0) (86, 0)}	{8, 8, 9, 8, 9}
7	{(8, 0) (17, 0) (26, 0) (35, 0) (44, 0) (52, 0) (61, 0)}	{9, 9, 9, 9, 8, 9}
	{(17, 0) (25, 0) (33, 0) (41, 0) (50, 0) (58, 0) (67, 0)}	{8, 8, 8, 9, 8, 9}
	{(26, 0) (34, 0) (42, 0) (50, 0) (59, 0) (67, 0) (76, 0)}	{8, 8, 8, 9, 8, 9}
	{(35, 0) (43, 0) (51, 0) (59, 0) (68, 0) (76, 0) (85, 0)}	{8, 8, 8, 9, 8, 9}
8	{(8, 0) (16, 0) (24, 0) (32, 0) (40, 0) (49, 0) (57, 0) (66, 0)}	{8, 8, 8, 8, 9, 8, 9}
	{(17, 0) (25, 0) (33, 0) (41, 0) (49, 0) (58, 0) (66, 0) (75, 0)}	{8, 8, 8, 8, 9, 8, 9}
	{(26, 0) (34, 0) (42, 0) (50, 0) (58, 0) (67, 0) (75, 0) (84, 0)}	{8, 8, 8, 8, 9, 8, 9}
9	{(8, 0) (16, 0) (24, 0) (32, 0) (40, 0) (48, 0) (57, 0) (65, 0) (74, 0)}	{8, 8, 8, 8, 8, 9, 8, 9}
	{(17, 0) (25, 0) (33, 0) (41, 0) (49, 0) (57, 0) (66, 0) (74, 0) (83, 0)}	{8, 8, 8, 8, 8, 9, 8, 9}
10	{(8, 0) (16, 0) (24, 0) (32, 0) (40, 0) (48, 0) (56, 0) (65, 0) (73, 0) (82, 0)}	{8, 8, 8, 8, 8, 8, 9, 8, 9}

nounced in BNNTs than in comparable CNTs because BNNTs reportedly possess lower transverse rigidity with ionic interaction between layers [43–45].

The simulations, conducted at T = 10 K, are addressing the minimum energy state of the system under a fixed strain. The reason for choosing low-T simulations is twofold: (i) the work substantially builds on and compares to first-principle T = 0 K calculations [4], as well as on the previous MD study on SW-BNNTs [21], which was also performed at T = 10 K; (ii) thermal effects lead to more complex behavior and would require a separate investigation, which is out of the scope of this research. Nevertheless, the implementation of the Sevik et al. [35] interatomic potential, which is shown to reproduce very well the phonon spectrum [35] and the thermomechanical properties [36] of a single hBN sheet, provides the possibility for applying the described simulation model also at elevated temperatures.

3. Simulation results

3.1. Equilibrium properties of multi-wall BNNTs

3.1.1. Potential energy of a multi-wall BNNT

A comparison of the potential energies between MW-BNNTs of different number of wall layers and tube diameters is essential in studying their relative distribution during synthesis. Fig. 4 compares the potential energies of all of the simulated BNNTs after relaxation at no load. The potential energies are given relative to the potential energy of a flat single sheet hBN, which for the Sevik et al. potential [35] is equal to −7.507 eV/atom.

The potential energies of SW-BNNTs ($L = 1$) include only the Tersoff potential and represent the strain energy of a folded hBN layer, which is positive and scales as $1/R^2$. Similar results for (m, m) SW-BNNTs were also reported by Singh et al. [36]. In addition to the strain energy, the potential energies of MW-BNNTs include the interwall interaction energy defined by the L-J potential in Eq. (5). Being attractive, this interaction adds a negative (compared to an isolated single hBN sheet) term to the potential energy. As a result, for a MW-BNNT of a radius above a certain crossover value, the potential energy will decrease when an additional wall-layer is added. As shown in Fig. 4, this happens at $R = 0.65$ nm for DW-BNNTs vs. SW-BNNTs, at $R = 1$ nm for 3W-BNNTs vs. DW-BNNTs, and at $R = 1.6$ nm for 4W-BNNTs vs. 3W-BNNTs, etc. Since BNNTs of lowest energy would be favored during synthesis, these crossing points of the potential lines of nanotubes

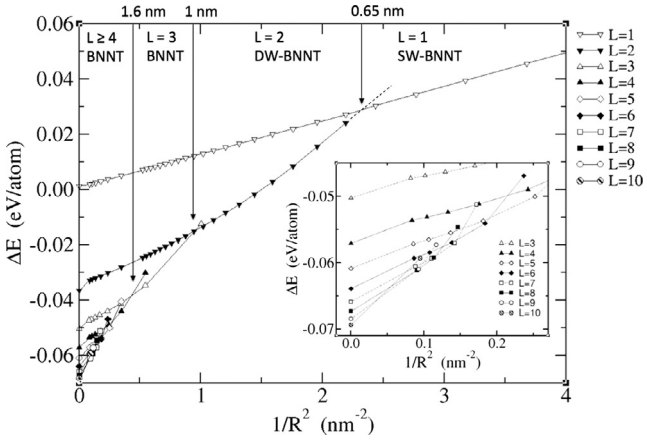

Fig. 4. Excess potential energy per atom, ΔE, as a function of the nanotube radius, R, of all of the simulated BNNTs of a given number of layers, L. $E = 0$ corresponds to a single flat hBN plane. The values at $1/R^2 = 0$ correspond to crystalline h-BN structures of L number of flat layers in equilibrium.

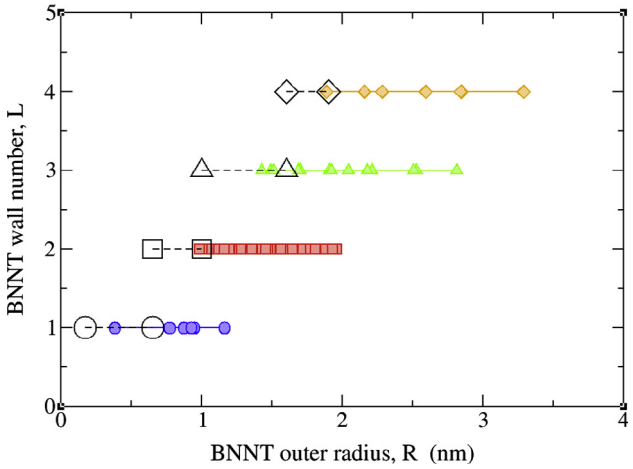

Fig. 5. Tube radius ranges for HTP-synthesized BNNTs of one to four walls (filled color symbols indicate individual measurements; the data are reproduced from [42]) plotted together with the range between the corresponding transition radii, obtained from the intersection points in Fig. 4 (large open symbols). (For interpretation of the references to colour in this figure legend, the reader is referred to the web version of this article.)

of the same L indicate the crossover radius between nanotubes of different number of layers. Thus, a nanotube of certain number of walls L, should have an energy-minimized radius between the crossing points corresponding to the transition from $L-1$ to L, and from L to $L + 1$.

A comparison of the predicted range of radii of transition, with the data from a set of HTP synthesized BNNTs [42], is given in Fig. 5. The details of the experimental setup and measurement are given in Section 4.1. The figure shows that while the MD results are not too far off from the experimental data, they tend to underpredict the radius range of the MW-BNNTs of a given number of walls. A possible reason for this is that the potential energy based analysis (at T = 10 K) does not account for the entropy at ambient temperatures and the kinematics of the growth mechanism under specific synthesis conditions. In addition, the prediction of the exact radius of transition relies also on the accuracy of the empirical potential used in the model.

3.1.2. Interlayer distances of multi-wall BNNTs

Interlayer distances have a substantial influence on the internal potential energy of MW-BNNTs. Because of the discrete atomic structure, the radius of an unstrained SW-BNNT can be only a discrete number of values, expressed through Eq. (6) for the $(m, 0)$-type nanotubes. Consequently, the geometrical interlayer distance h_l between two adjacent layers l, and $l + 1$, of indices $(m_l, 0)$ and $(m_{l+1}, 0)$ in a MW-BNNT is expressed through Eq. (7). The van der Waals forces acting between the layers dictate that h_l must be close to the equilibrium interplanar distance of an hBN crystal, $h_0 = 0.333$ nm. As discussed in Section 2.3, this is achieved for $\Delta m_l = 8$ or 9, giving two possible values for h_l in Eq. (7), as: $h_l = 0.318$ nm, and $h_l = 0.358$ nm, respectively. Fig. 6 is a plot of the h_l values vs. the radius of the l-th layer, $R_l = R_{(m_l,0)}$ for all $\{(m_l, 0); l = 1, 2, \ldots L-1\}$ combinations of nanotubes for $L \geqslant 2$ listed in Table 4. One can see that a split of h_l towards 0.32 and 0.35 nm occurs at small $R_l < 1$ nm, which disappears at $R_l > 2$ nm, where h_l converges to h_0. The inset in Fig. 6 emphasizes this split between h_1 and h_2 for 3W-BNNTs compared to h_1 for DW-BNNTs. The split is most pronounced at small radii ($R_l < 2$ nm), because the difference between h_l at $\Delta m_l = 8$, and $\Delta m_l = 9$, is most difficult to be accommodated in thin nanotubes. From Table 4 one can see that as the nanotube radius grows, the preferred index change, Δm, between consecutive layers goes from 9, for L < 5, to

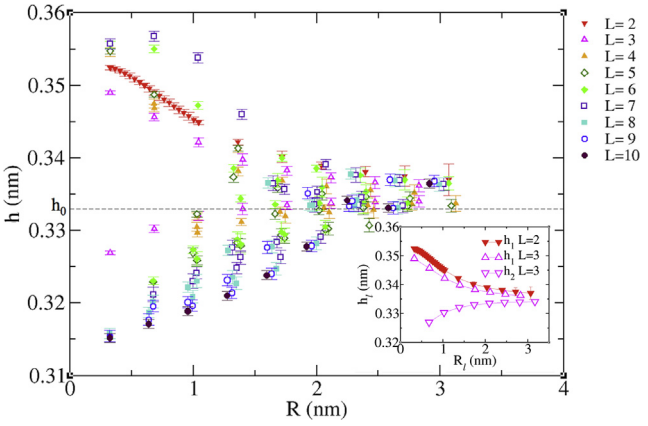

Fig. 6. Interlayer distances h_l between the l-th and the $l+1$ layer in a L-wall BNNT as a function of the radius of the l-th layer R_l. (For interpretation of the references to colour in this figure legend, the reader is referred to the web version of this article.)

8 for L ≥ 5, indicating that in thicker nanotubes accommodating h_l at $\Delta m_l = 8$, becomes preferable to h_l at $\Delta m_l = 9$.

3.1.3. Spontaneous polarization of multi-wall BNNTs

Spontaneous, or preexisting permanent polarization of BNNTs, has been first suggested by Mele and Král [3] as a pure quantum mechanical effect, arising from braking the hexagonal symmetry of the hBN layer when it is folded into a nanotube and the need to satisfy quantum mechanical boundary conditions around the tube circumference. A classical empirical model cannot, by its nature, emulate fully and correctly such an effect, but it can emulate part of it, particularly the part that is due to the hexagonal symmetry breaking, but not due to the circumference boundary conditions of the electronic states. With this in mind, as demonstrated previously [21], the piezoelectric model from Eq. (1) predicts a polarization of the hBN layer in bending mode, which leads to a spontaneous polarization per unit cell of an unloaded SW-BNNT equal to [21]

$$p_{bend} = \frac{C}{R^2} \quad \text{with} \quad C = \frac{p_0}{64\sqrt{3}}(1 - 27t_\theta) \tag{8}$$

The fitting values for p_0 and t_θ from Table 1 give $C = 0.006$ (e × nm). This bending polarization becomes comparable to the strain induced piezoelectric polarization only for very small $R \ll 1$ nm, and is not expected to have a significant role in MW-BNNTs.

In MW-BNNTs, spontaneous polarization can be induced by an additional mechanism. As noted in Section 3.1.2, the deviation of the interlayer distance, h_l, from h_0 in MW-BNNTs creates incompatibility strain in the BNNT layers. Fig. 7(a) shows an example of the radial strain $\varepsilon_{l,RR}$ in two simulated 9W- and 10W-BNNTs,

$$\varepsilon_{l,RR} = (R_l - R_{l,0})/R_{l,0}, \tag{9}$$

for each layer $l = 1, 2, \ldots L$ of radius R_l relative to the equilibrium radius, $R_{l,0}$, calculated through Eq. (6) using the relevant $(m, 0)$ index for that layer (see Table 4, L = 9 and 10). If one imagines a nanotube layer being unrolled as a flat hBN sheet in the x-y plane, this strain is equivalent to an inplane strain, ε_{yy}, perpendicular to the axial x-direction. According to Eq. (2), ε_{yy} induces an axial polarization per unit cell p_x equal to:

$$p_x = e_{xyy}\varepsilon_{yy} = -\frac{p_0}{2\sqrt{3}r_0^2}[(1 + A) - 3t_\theta(1 - A)]\varepsilon_{yy}. \tag{10}$$

This polarization, together with the bending polarization from Eq. (8), leads to an overall polarization of the l-th layer $P_l = p_x + p_{bend}$, given as

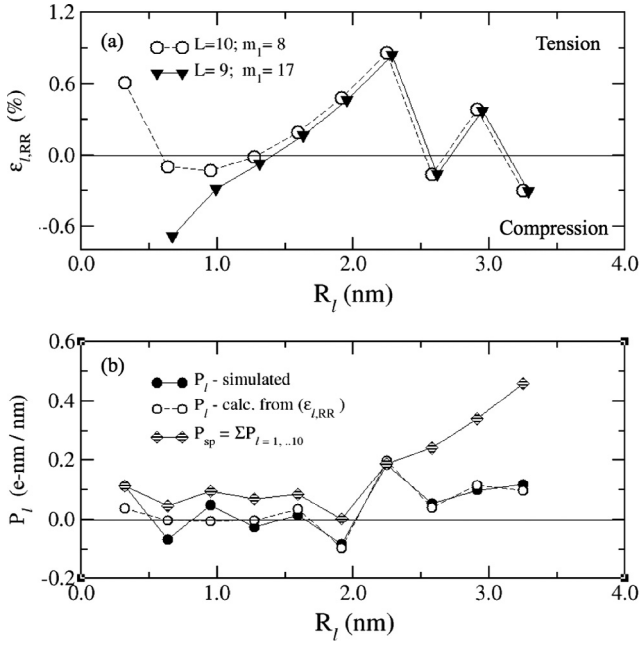

Fig. 7. (a) Radial strain $\varepsilon_{l,RR}$ of the l-th layer Eq. (7) in a nine- and a ten-wall BNNT of length 1 nm as a function of its radius, R_l. (b) Spontaneous polarization of the l-th layer P_l obtained with the $\varepsilon_{l,RR}$ given in (a) for the ten-wall BNNT. Symbols indicated values that were: ● - simulated; ○ - calculated from Eq. (9); ◇ - cumulative polarization over l layers.

$$\begin{aligned} P_l &= (-1)^l\left(p_x + \frac{C}{R_l^2}\right)\Omega N_l \\ &= (-1)^{l-1}\left\{\frac{3p_0}{8}[(1 + A) - 3t_\theta(1 - A)]\varepsilon_{yy} + \frac{C\Omega}{R_l^2}\right\}N_l. \end{aligned} \tag{11}$$

Here, the $(-1)^l$ factor accounts for the alternating direction of the B—N bond in each consecutive layer in the AA' stacking sequence, which leads to an alternating polarization direction in each layer. The symbol $\Omega = \frac{3\sqrt{3}}{4}r_0^2 = 0.027$ nm^2, is the area per atom in the hBN lattice, and N_l is the number of atoms in the l-th layer.

Fig. 7(b) shows the measured overall l-th layer polarization $P_l(l = 1, \ldots 10)$ from the simulation of the 10W-BNNT, together with the calculated values from Eq. (11) using the estimated strain values, $\varepsilon_{l,RR}$, as given in Fig. 7(a). For consistency, the polarization values are scaled for $H = 1$ nm length of the nanotube (i.e., N_l in Eq. (11) is taken for a layer of a 1 nm-long nanotube). One can see that Eq. (11) closely reproduces the simulated polarization for $R_{l>3} > 1$ nm, and starts to deviate for $R_{l\leqslant 3} \leqslant 1$ nm. This shows that as the layer curvature increases, additional factors begin to dominate the polarization. One factor is the breaking of the B—N overlap in the AA' stacking between adjacent layers as the layer bending increases, leading to additional local interlayer forces that may change the local strain and, consequently, the polarization.

The overall spontaneous polarization of a MW-BNNT is the sum of the polarizations of each layer, $P_{sp} = \sum_{l=1}^{L} P_l$. This cumulative sum is given in Fig. 7(b) for the 10W-BNNT. The estimated P_{sp} for all of the simulated nanotubes is presented in Fig. 8. Following the data points for each L, a few trends could be identified. The P_{sp} of the SW-BNNTs follows the $1/R^2$ law, as expected from Eq. (11), with an estimated fitted pre-factor, $C\Omega = 0.004e \times nm$. The $1/R^2$ dependence is not followed by the MW-BNNTs, because the polarization of the individual layers, P_l, becomes dominated by the incompatibility strain, $\varepsilon_{l,RR}$ in Eq. (9), which enters as ε_{yy} in Eq. (11) and increases the contribution of the first term in this

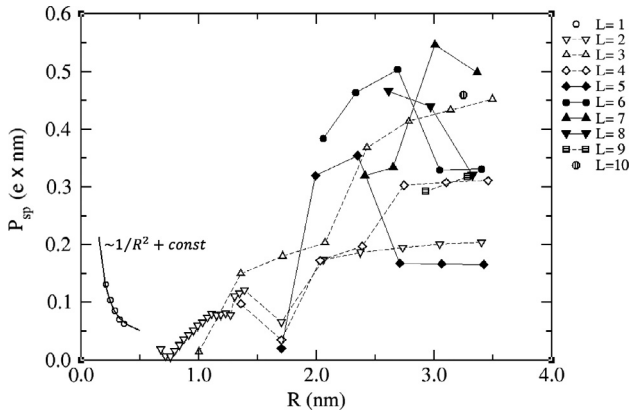

Fig. 8. Total simulated spontaneous polarization of unstrained multiwall BNNTs of L layers as a function of the nanotube radius, R. The data are given for BBNTs of 1 nm length.

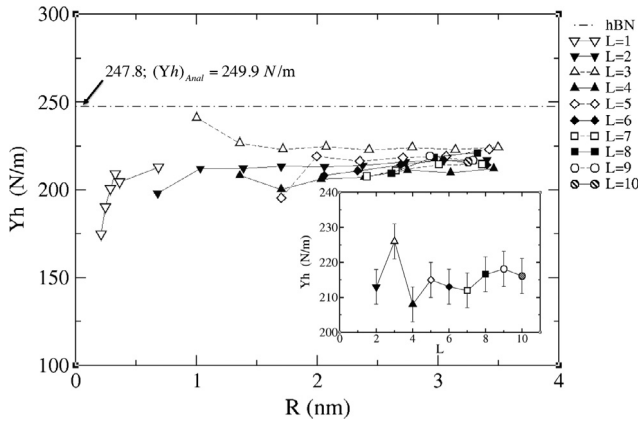

Fig. 9. Young's modulus, Y, multiplied by interlayer distance, h, for all of the simulated BNNTs as a function their radius, R, and number of wall layers, L. The inset gives the mean values of Yh averaged for $R < 3.5$ nm for each $L > 1$.

equation. As a result, the MW-BNNTs of low number of layers, $L < 5$ (open symbols in Fig. 8), show a continuous increase of their polarization as the radius increases. The MW-BNNTs of higher number of layers, $5 \leqslant L < 9$, show a peak in their polarization at intermediate radius, $2 < R_{peak} < 3$ nm, followed by a decrease. The data for $L = 5, 6,$ and 7 indicate that the peak radius drifts towards larger R as L increases. A peak radius is not observed for $L = 8, 9$ and 10, likely because the simulations were limited to nanotubes of $R < 3.5$ nm. Still, the data for $L = 8$ suggests that the peak has already been passed, while for $L = 9$, it is yet to be reached, consistent with the expectations of an increasing peak radius with L. These results suggest that MW-BNNTs could sustain significant electric charge, experiencing stronger electrostatic interactions than van der Waals forces alone. To put this into perspective, after taking into account the estimated direct piezoelectric coefficient in Section 3.2.2, the spontaneous polarization of a 7W-BNNT of 3 nm in radius (the highest point in Fig. 8) is equivalent to the polarization of a 1.4% pre-strained nanotube. One consequence of this spontaneous polarization phenomenon is that it increases the van der Waals forces acting between the nanotubes. As a result, while BNNTs with radii of around 3 nm may be more difficult to disperse in solutions, they may be more likely to form strong tightly-bound bundles and fibers.

3.2. Mechanically loaded multi-wall BNNTs

3.2.1. Elastic properties of a multi-wall BNNT

Analytical expressions for the elastic properties of BNNTs were given by Song et al. [33] in terms of the spatial derivatives of the interatomic potential. To recall, the two-dimensional tensile stiffness of a hBN monolayer, expressed as a product of the Young's modulus, Y, and the interlayer distance, h, is

$$Yh = \frac{B}{4\sqrt{3}} \frac{\left(\frac{\partial^2 V}{\partial r^2}\right)_0}{\left(\frac{\partial^2 V}{\partial r^2}\right)_0 + \frac{B}{8}} \tag{12}$$

The parameter B in Eq. (12) is defined through the interatomic potential V, acting between two atoms at distance r, and its spatial derivatives at equilibrium (noted by the '0' subscript) [33]. For the Tersoff potential [35], the value of B is given in Table 1, which with the calculated $\left(\frac{\partial^2 V}{\partial r^2}\right)_0 = 3926.6$ (eV/nm^2) gives $Yh = 1561.9$ (eV/nm^2) $= 249.9$ (N/m).

Young's modulus of the simulated BNNTs was determined by fitting the change of the potential energy per unit volume ΔE_p of an isolated nanotube to a quadratic dependence of the applied uniaxial strain ε_{xx} as

$$\Delta E_p = \frac{1}{2} Y \varepsilon_{xx}^2. \tag{13}$$

The Yh values for all of the simulated BNNTs are plotted in Fig. 9. The inset gives the averaged values of Yh for $R < 3.5$ nm for each L. The data show some oscillations, which are more pronounced at small L and decreased at larger L. These oscillations are likely due to the incompatibility strain between layers, as discussed in Section 3.1. The mean of the oscillations is around $Yh \approx 215 \pm 5$ (N/m) ($Y \approx 645 \pm 15$ GPa), which is lower than the analytical value calculated from Eq. (12). A controlled simulation of a crystalline hBN gives $Yh = 247.8$ (N/m) – very close to the analytical value – suggesting that the lower elastic coefficient for BNNTs is likely due to the folding of the hBN layers into a nanotube.

For a SW-BNNT of length H and radius R, the tensile stiffness, k, is equal to [33]

$$k^{SW} = \frac{YS^{SW}}{H} = Yh\frac{2\pi R}{H} = 1570.2\frac{R}{H} \text{ (N/m)} \tag{14a}$$

where $S^{SW} = 2\pi Rh$ is the cross-sectional area of the wall of thickness h of a SW-BNNT.

For a MW-BNNT, consisting of L nanotube layers of radii $(R_1, R_2, \ldots, R_L)$, the tensile stiffness is equal to [33]

$$k^{MW} = \frac{YS^{MW}}{H} = \frac{2\pi}{H}(R_1 + R_2 + \ldots + R_L)Yh. \tag{14b}$$

An alternative to Eq. (14b) can be obtained if S^{MW} – the cross-sectional area of all BNNT wall layers – is expressed through the inner and outer radii of the BNNT, R_1, and R_L, respectively (Fig. 3) as

$$\begin{aligned} S^{MW} &= \pi[(R_L + h/2)^2 - (R_1 - h/2)^2] \\ &= \pi[R_L^2 - R_1^2 + h(R_L + R_1)]. \end{aligned} \tag{15}$$

The above expression naturally transforms into S^{SW} in Eq. (14a) when $R_L = R_1 = R$ and in the case of a very thin nanotube of $R = h/2$, it gives the base area of a full cylinder, $S = \pi h^2$. Furthermore, for the case of a MW-BNNT of radius $R = R_L$, assuming an equidistant spacing of the layers, $h_l = h = constant$, one can write $R_1 = R - (L-1)h$, which leads to a generalized expression for S^{MW}:

$$S^{MW} = \begin{cases} \pi L[2R - (L-1)h]h; & R > h/2 \\ \pi h^2; & R \leqslant h/2 \end{cases}. \tag{16}$$

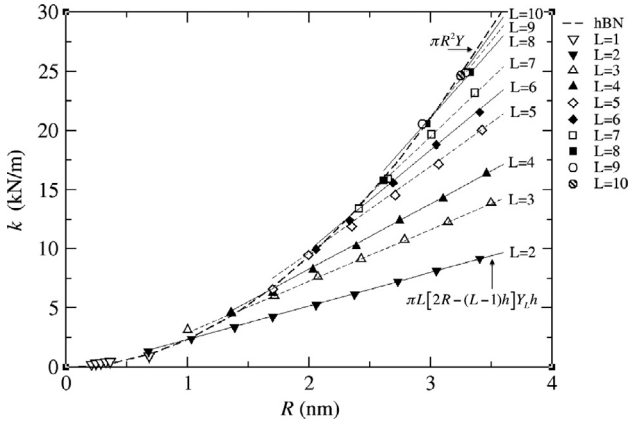

Fig. 10. Tensile stiffness, k, of MW-BNNTs as a function of their radius, R, and number of layers, L. Symbols indicate simulated data, lines indicate the corresponding analytical values calculated using Eq. (17) with H = 1 nm, and Yh values from the inset in Fig. 9.

Consequently, the tensile stiffness is:

$$k^{MW} = \frac{YS^{MW}}{H} = \frac{Yh}{H} \times \begin{cases} \pi L[2R-(L-1)h]; & R > h/2 \\ \pi h; & R \leqslant h/2 \end{cases}, \tag{17}$$

with Yh determined from Eq. (12).

Eq. (17) explains well the simulation results shown in Fig. 10. The stiffness of nanotubes of equal L shows the predicted linear dependence of R, with a slope, dependent on L. The upper envelope of the data gives the limiting case of fully filled nanotubes, having the stiffness of a full hBN cylinder of radius R, and base area, $S = \pi R^2$.

3.2.2. Direct piezoelectric effect of a multi-wall BNNT

The direct piezoelectric effect is the effect of induced polarization under an applied strain. In this work, this effect is studied by measuring the dipole moment per unit cell p_{cell}, induced under tension (stretching) applied along the tube axis, $\varepsilon_s = \varepsilon_{xx}$:

$$p_{cell} = e_{xxx}(1+\nu)\varepsilon_{xx} = e_{11}\varepsilon_s, \tag{18}$$

where $e_{11} = e_{xxx}(1+\nu)$ is the tensile piezoelectric coefficient of the nanotube [21], and e_{xxx} is expressed through Eq. (2). Using the values of e_{xxx} and ν from Table 1, $e_{11} = 2.14$ e/nm $= 3.42 \times 10^{-10}$ C/m. This value is in close agreement with the DFT calculations [46], reported as 3.71×10^{-10} C/m for a "clamped-ion" hBN monolayer.

The piezoelectric polarization of the l-th nanotube layer in a MW-BNNT of L layers is

$$p_l = p_{cell}S_l = e_{11}S_l\varepsilon_s = e_{11,l}\varepsilon_s, \tag{19}$$

where $S_l = 2\pi R_l H$ is the circumferential area of the l-th layer, and $e_{11,l}$ is the piezoelectric coefficient defined for that layer. The piezoelectric coefficient for the whole nanotube is the sum over all layers

$$e_{11,L} = \sum_{l=1}^{L}(-1)^{l-1}e_{11,l} = 2\pi e_{11}\sum_{l=1}^{L}(-1)^{l-1}R_l H, \tag{20}$$

where, as in Eq. (11), the $(-1)^{l-1}$ factor accounts for the alternating direction of the B—N bond in each layer in the AA' stacking sequence. Assuming equidistant spacing of the layers, $h_l = h = constant$, the radius of the l-th layer can be expressed as $R_l = R - (L-l)h$, which when substituted in Eq. (20) yields

$$e_{11,L} = 2\pi e_{11}H\sum_{l=1}^{L}(-1)^{l-1}[R-(L-l)h]. \tag{21}$$

Because of the alternating direction of the polarization in consecutive layers, nanotubes of even and odd number of layers will have substantially different piezoelectric polarization.

For nanotubes of even number of layers, $L = 2n$:

$$e_{11,L}^{even} = 2\pi e_{11}H\sum_{l=1}^{n}\{[R-(2n-l)h]-[R-(2n-l-1)h]\} = -\pi Lhe_{11}H. \tag{22a}$$

For nanotubes of odd number of layers, $L = 2n+1$:

$$e_{11,L}^{odd} = 2\pi Re_{11}H + e_{11,L-1}^{even} = \pi[2R-(L-1)h]e_{11}H. \tag{22b}$$

Note that the polarization coefficient of the even-layer nanotubes does *not* depend on the nanotube radius, while for the odd-layer nanotubes, there is a linear dependence of R, at given L. The negative sign in Eq. (22a) is due to the predefined choice of the exponent of the (-1) factor in Eq. (20), setting the polarization coefficient of a SW-BNNT (or the innermost layer of a MW-BNNT) as positive. In this sense, the sign in Eq. (22a) means that the polarization of an even-layer nanotube will have the sign of the outermost layer, which is negative relative to the innermost layer, since it has the largest radius and the largest circumferential area of all layers.

The estimated magnitude of the piezoelectric coefficients of all of the simulated nanotubes normalized for $H = 1$ nm, is given in Fig. 11. The data clearly differentiate the even-layer nanotubes, with a piezoelectric coefficient independent of R, from the odd-layer nanotubes, showing a linear increase of the polarization with R, as expected from Eq. (22b). In addition, again in agreement with Eqs. (22a) and (22b), for a fixed radius $R = constant$, and increasing L, the polarization of even-layer nanotubes *increases*, while that for the odd-layer nanotubes *decreases*.

3.2.3. Converse piezoelectric effect of a multi-wall BNNT

The converse piezoelectric effect, also referred as the inverse piezoelectric effect, is the effect of induced strain under an applied external electric field. When the electric field, U_x, is applied along the tube axis oriented in the x-direction, the coefficient of proportionality, d_{11}, between U and the inducing stretching, ε_s, is the converse piezoelectric coefficient:

$$\varepsilon_s = d_{11}U_x. \tag{23}$$

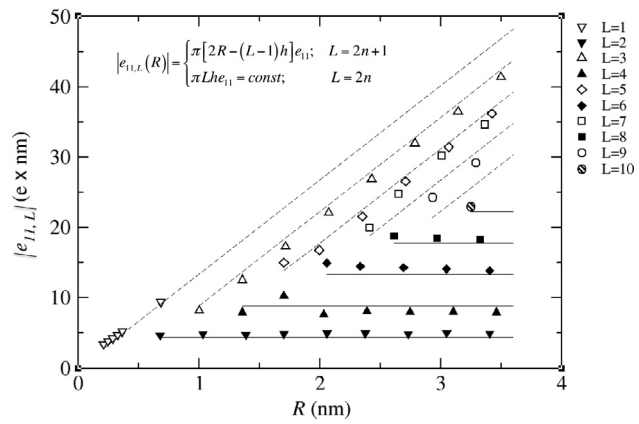

Fig. 11. The total direct piezoelectric coefficient in stretching $e_{11,L}$ for all simulated MW-BNNTs as a function of their radius, R, and the number of layers, L. The simulated data (symbols) are plotted together with the analytical dependence Eq. (22) (lines) for nanotubes of odd number of layers L (open symbols – dashed lines), and of even number of layers L (full symbols – solid lines). The data are normalized for nanotubes of 1 nm length.

The converse piezoelectric effect is not explicitly simulated in this work, but it can be deduced from the direct piezoelectric effect in combination with the elastic properties of MW-BNNTs as studied in Sections 3.2.1 and 3.2.2, assuming that the underlying mechanism for the converse piezoelectricity is the same as for the direct piezoelectricity. The relation between the converse and the direct piezoelectric coefficients is:

$$d_{11} = \frac{\overline{e_{11}}}{Y}. \tag{24}$$

In Eq. (24), $\overline{e_{11}}$ is the direct piezoelectric coefficient in tension per unit nanotube volume. In Section 3.2.2, it was shown that the piezoelectric response of a MW-BNNT is not uniform throughout the volume, but has a complex structure due to the AA' stacking. For this reason, $\overline{e_{11}}$ for a MW-BNNT is defined as the volume average, $\overline{e_{11}} = e_{11,L}/S^{MW}H$, giving

$$d_{11} = \frac{e_{11,L}}{YS^{MW}H}. \tag{25}$$

Using the values of $e_{11,L}$ from the simulations as given in Fig. 11, together with Y from Fig. 9, d_{11} can be determined for all of the considered MW-BNNTs. The results are plotted in Fig. 12.

An analytical expression for d_{11} can be derived from Eq. (25) after substituting S^{MW} and $e_{11,L}$ from Eq. (15b), and Eqs. (22a) and (22b), which gives:

$$d_{11}^{even} = \frac{-e_{11}}{[2R-(L-1)h]Y}; \quad L = 2n, \tag{26a}$$

$$d_{11}^{odd} = \frac{e_{11}}{LhY}; \quad L = 2n+1. \tag{26b}$$

As in Eq. (22a), the negative sign in Eq. (26a) indicates that the polarization of an even-layer nanotube will have the sign of the outermost layer, while the innermost layer polarization is considered positive to be consistent with the SW-BNNT case.

For dimensional considerations, note that e_{11}, as defined through Eq. (18), is the two-dimensional piezoelectric coefficient of a hBN monolayer per unit area, while d_{11} is the three-dimensional converse piezoelectric coefficient per unit volume of the nanotube. If e_{11} is expressed in 10^{-10} C/m, R and h in Å, and Y in TPa, then d_{11} is obtained in pm/V or $(\mathrm{m/V} \times 10^{-12})$.

A comparison between the analytical and the simulated values of d_{11} is given in Fig. 12. For even-layer nanotubes, the simulated

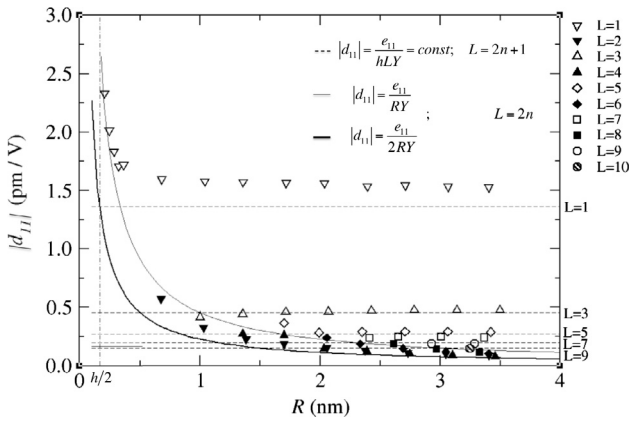

Fig. 12. The converse piezoelectric coefficient d_{11} for all simulated MW-BNNTs as a function of their radius, R, and the number of layers, L. The simulated data (symbols) are plotted together with the analytical dependence Eq. (26) (lines) for nanotubes of odd number of layers L (open symbols – dashed lines), and of even number of layers L (full symbols – solid lines). The data are normalized for nanotubes of 1 nm length.

d_{11} shows no distinguishable dependence on L, while following a general $1/R$ behavior, and bonded by the e_{11}/RY and $e_{11}/2RY$ curves. This is in agreement with Eq. (26a), which is dominated by the $e_{11}/2RY$ when $Lh \ll R$, and by e_{11}/RY when $Lh \to R$. The former case is representative for hollow nanotubes (e.g., Fig. 2(e)), while the latter case is representative for full nanotubes (e.g., Fig. 2(f)). The d_{11} for odd-layer nanotubes of $L > 1$ closely follows the relation in Eq. (26b), which scales as $1/L$, independent of R. SW-BNNTs ($L = 1$) approach the analytical solution for $R > 1$ nm, but diverge strongly at $R < 0.5$ nm. The deviation is due to the rapid decrease of Yh when $R < 0.5$ nm (Fig. 9). This divergence approaches the analytical line e_{11}/RY for full nanotubes (as nanotubes of $R \to h/2$ can be considered full nanotubes), which follows from both Eqs. (26a) and (26b) when $Lh \to R$, i.e.,

$$d_{11}^{odd,even}\Big|_{Lh\to R} \to \frac{\pm e_{11}}{RY}. \tag{27}$$

For $R \gg h/2$, Fig. 12 gives d_{11} for the SW-BNNTs ($L = 1$) approaching 1.5 pm/V. This value is in agreement with the DFT results [46] of 1.50 pm/V for a "clamped-ion" hBN monolayer. The estimated d_{11} values for MW-BNNTs are all below 0.5 pm/V, which is substantially lower than the SW-BNNT values due to the alternating polarization of the consecutive wall layers in the AA' stacking.

Recent measurements of a 40 wt% BNNT/polymer composite [8] reported a piezoelectric coefficient d_{13} of 14.41 pm/V, which is significantly higher than the calculated values reported above for an isolated BNNT. To reconcile this substantial difference between an isolated BNNT and a BNNT/polymer composite, one needs to correctly estimate the overall piezoelectric properties, as well as the overall stiffness of the composite, which does not always follow the simple rule of mixtures. One needs to account for the physical interaction of the BNNTs with the dielectric polymer matrix that leads to non-linear effects. One example of these effects is the appearance of interfacial polarization, which is known to be a mechanism for enhanced piezoelectric behavior of heterogeneous composites. Other possible mechanisms that affect piezoelectric properties of a composite include: (i) the inter-tube interaction of BNNTs via the dielectric medium; (ii) the random coiled morphology of the nanotubes in the composite leading to redistribution of the BNNTs polarization; (iii) appearance of defects in the BNNTs with enhanced dipole moments, and others. Further study is needed for those more complicated systems.

4. BNNT fiber

In this section, the derived analytical expressions in Section 3 for the elastic and piezoelectric properties of isolated BNNTs will be used to predict the physical properties of an example system, representing a BNNT fiber composed of BNNTs with an experimentally established diameter and wall number distribution.

4.1. Experimental characterization of BNNT distribution

The BNNTs used for this example were synthesized using the HTP method [25,34] and were characterized by AFM. Prior studies have revealed that HTP-synthesized BNNTs are highly crystalline, up to 100 μm in length, and less than 10 nm in diameter. The HTP-BNNTs were found to be predominantly 1-to-4 walled nanotubes with a dominant presence of double-walled structures as shown in high resolution transmission electron microscope (HRTEM) images in Fig. 13. For AFM measurements of BNNT diameters, as-synthesized BNNTs were first separated and dispersed in deionized (DI) water by means of ultrasonication with the aid of ionic surfactants [42,43]. After centrifugation at 2000 rpm for

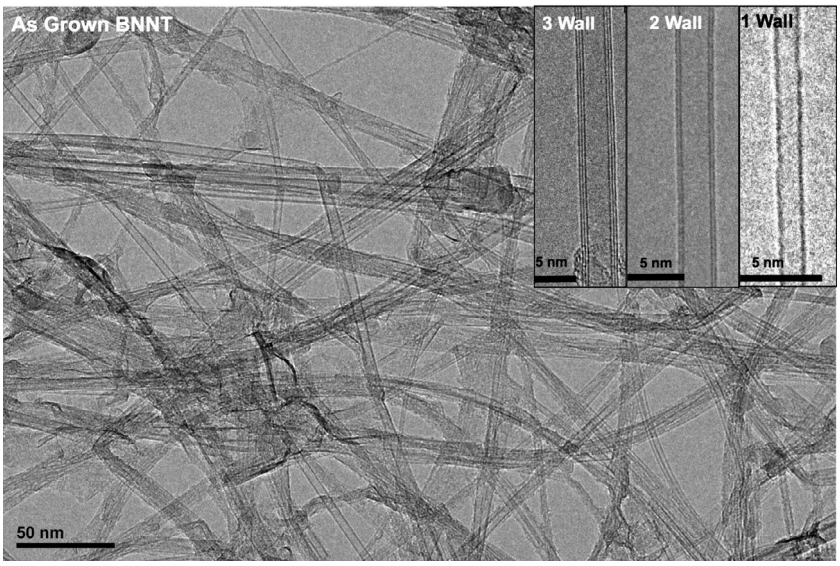

Fig. 13. TEM image of as grown boron nitride nanotubes with close views of 1-wall, 2-wall, and 3-wall nanotubes shown in the insets.

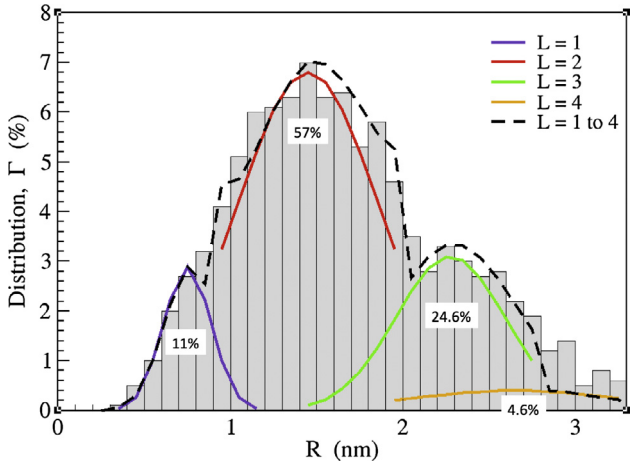

Fig. 14. Histogram of the outer diameter distribution based on AFM measurements of 1000 randomly selected individual HTP-grown BNNTs. The solid curves are the respective Gaussian fitting curves corresponding to different wall layers, L, as indicated. The percentage of each type of tubes is calculated as the area under the respective fitting curves. The black dashed line is the aggregate fitting curve. (For interpretation of the references to colour in this figure legend, the reader is referred to the web version of this article.)

30 min, small drops from the top portion of the BNNT solution were deposited on clean Si wafers. The deposited BNNT samples were subsequently rinsed with DI water to remove residue surfactants, and then air-dried. The cross-sectional heights of individual BNNTs on the substrate, Δh, were measured using a Park Systems XE-70 AFM. The AFM operated in a tapping mode with silicon probes of less than 10 nm in nominal tip radius in ambient environment. The tubes outer diameters were calculated as $D^{out} = \Delta h - h$, where $h = 0.34$ nm is the inter-layer distance of the B—N sheet.

Fig. 14 shows the outer radius distribution that is obtained based on the AFM measurements of $N_{fiber} = 1000$ individual BNNTs that were randomly selected. To quantify the probability distribution of the wall numbers of the tubes, it is assumed that the radius distribution of BNNTs with a certain wall number follows a Gaussian distribution. This assumption is consistent with the observed distributions based on the HRTEM measurements of 77 BNNTs of 1-4 tube walls, which were originally reported [42] and are reproduced and displayed in Fig. 5. The HRTEM-measured radius range of each type of tube is utilized in the Gaussian fitting of the BNNT radius distribution histogram. The Gaussian fitting starts from the data with the smallest radius values, which are considered to correspond to single-walled tubes, and moves towards the data with higher radius values that are for tubes of higher wall numbers. The solid curves shown in Fig. 14 are the respective fitting curves for SW- to 4W-BNNTs, through which the fraction of tubes $n_L(R)$ of type L, having radius between $R - \Delta R/2$ and $R + \Delta R/2$ with $(\Delta R = 0.1$ nm$)$ is expressed as

$$n_L(R) = n_{0,L} \exp\left[-\frac{(R - \bar{R}_L)^2}{\sigma_L^2}\right], \tag{28}$$

where $n_{0,L}$ is the maximum of the distribution, $\bar{R}_L$ is the mean radius, and σ_L is the standard deviation. Their fitted values are given in Table 5.

The dashed line displayed in Fig. 14 represents the aggregated fitting curve that is obtained through the summation of all four individual fitting curves and shows a reasonable agreement with the AFM-measured radius distribution histogram. The percentage of each type of tube is calculated as the area fraction under the respective fitting curve and is found to be 11.0% (SW), 57.0% (DW), 24.6% (3W) and 4.6% (4W). The analysis shows that DW BNNTs have a dominant presence in the HTP-synthesized BNNTs, and more than 97% of the tubes are SW- to 4W-BNNTs. The results based on the AFM measurements are consistent with the prior HRTEM observations of the BNNT radius and wall number distributions [25,42].

4.2. Elastic properties of a BNNT fiber

Assuming that a fiber is prepared from the BNNT conglomerate examined in Section 4.1 and all tubes are perfectly aligned, one can use the Gaussian distribution $n_L(R)$ from Eq. (28) with the estimated parameters from Table 5 to calculate the total fiber stiffness as

$$k_{fiber} = N_{fiber} \sum_{L=1}^{4} k_L \tag{29}$$

with

Table 5
Fitted parameter values, $n_{0,L}$, $\bar{R}_L$, and σ_L, of the Gaussian distribution in Eq. (28) of a BNNT aggregate, together with the relative molecular fraction, and the volume fraction of each LW BNNT type. Young's modulus, expressed as $Y_L h$, and the partial stiffness per one nanotube, k_L, integrated analytically by Eq. (30b) for each L-type are also given.

L	$n_{0,L}$ (%)	$\bar{R}_L$ (nm)	σ_L (nm)	Mol. fraction (%)	Volume fraction (%)	$Y_L h$ (N/m)	k_L (N/m)
1	2.9	0.75	0.20	11.0	1.8	200	97
2	6.8	1.45	0.60	57.0	49.2	215	2501
3	3.1	2.275	0.45	24.6	39.0	225	2034
4	0.4	2.65	0.85	4.6	10.0	210	684

$$k_L = \frac{1}{R}\int_0^\infty k_L^{MW}(R) n_L(R) dR. \tag{30a}$$

Above, k_L is the partial stiffness, or the stiffness of the fraction of LW BNNTs, and $k_L^{MW}(R)$ is the stiffness of an isolated nanotube of radius R, expressed through Eq. (17). Integration of Eq. (30a), using Eq. (28) for $n_L(R)$, gives (see Appendix)

$$k_L = n_{0,L}\frac{Y_L h}{H\Delta R}\pi^{3/2}\sigma_L L[2\bar{R}_L - (L-1)h] = \frac{1}{\Delta R} n_{0,L}\sqrt{\pi}\sigma_L k_L^{MW}(\bar{R}_L). \tag{30b}$$

As seen from Fig. 9, the MD simulations show that Y varies slightly for nanotubes of different R and L. To simplify the integration in Eq. (30a), the $Y(R)$ dependence was averaged for each L, as shown in the inset to Fig. 9, and used as a constant, Y_L, in Eq. (30b). Table 5 gives the MD-values of $Y_L h$, and the calculated values of $k_L (L = 1, \ldots 4)$ for $H = 1$ nm BNNTs. The total stiffness for a fiber of $N_{fiber} = 1000$ according to Eq. (29) is $k_{fiber} = 5.3$ MN/m.

Knowing k_{fiber}, one can calculate the overall Young's modulus for the considered BNNT fiber using the relation

$$(Yh)_{fiber} = \frac{k_{fiber}}{S_{fiber}} Hh, \tag{31}$$

where S_{fiber} is the total base area of the BNNT fiber. S_{fiber} can be calculated as a sum of the base areas of all BNNTs in the fiber, divided by some packing coefficient, C_{pack},

$$S_{fiber} = \frac{N_{fiber}}{C_{pack}}\sum_{L=1}^{4} S_L^{Base} \tag{32}$$

with

$$S_L^{Base} = \frac{1}{\Delta R}\int_0^\infty \pi R^2 n_L(R) dR, \tag{33a}$$

being the base area contributed by the L-wall BNNTs. Here, the base area of a BNNT, equal to πR^2, should not be confused with the cross-sectional area of the BNNT layers, S^{MW}, as defined through Eqs. (14)–(16).

Integrating Eq. (33a) gives (see Appendix)

$$S_L^{Base} = \frac{1}{\Delta R} n_{0,L}\pi^{3/2}\sigma_L\left(\frac{1}{2}\sigma_L^2 + \bar{R}_L^2\right). \tag{33b}$$

Knowing S_L^{Base}, one can estimate the volume fraction of the L-wall BNNTs defined as $S_L^{Base}/\sum_{L=1}^4 S_L^{Base}$ and given in Table 5.

After choosing the packing coefficient in Eq. (32) as $C_{pack} = 0.8$[2] (an intermediate value between 0.907 for dense hexagonal packing of cylinders, and 0.75 for square packing), the calculated cross-section of the BNNT fiber is $S_{fiber} = 13150$ nm^2, and the overall Young's modulus of the fiber from Eq. (31) is $(Yh)_{fiber} = 137$ N/m, or $Y_{fiber} = 410$ GPa.. This value is 55% of the theoretical Young's modulus for an hBN sheet defined by Eq. (12), while still assuming perfect crystallinity of the BNNTs. The decreased Young's modulus of the fiber is mainly due to its lower density compared to a crystalline hBN.

The mass density of the fiber can be calculated as

$$\rho_{fiber} = \frac{N_{fiber}\sum_{L=1}^4 S_L^{cross}}{S_{fiber}}\rho_{hBN}, \tag{34}$$

where ρ_{hBN} is the mass density of a crystalline hBN, and

$$S_L^{cross} = \frac{1}{R}\int_0^\infty S_L^{MW}(R) n_L(R) dR, \tag{35}$$

where S_L^{MW} is the cross-section area given by Eq. (16).

Integration of Eq. (35) is identical to the integration of Eq. (30a), because $k_L^{MW}(R) = \frac{Y_L}{H} S_L^{MW}(R)$, giving

$$S_L^{cross} = n_{0,L}\frac{h}{\Delta R}\pi^{3/2}\sigma_L L[2\bar{R}_L - (L-1)h]. \tag{36}$$

Inserting Eq. (36) in Eq. (34) and using Eq. (32) and Eq. (33b) to express S_{fiber}, the fiber density is

$$\begin{aligned}\rho_{fiber} &= h\frac{\sum_{L=1}^4 n_{0,L}\sigma_L L[2\bar{R}_L - (L-1)h]}{\sum_{L=1}^4 n_{0,L}\sigma_L\left(\frac{1}{2}\sigma_L^2 + \bar{R}_L^2\right)} C_{pack}\rho_{hBN} \\ &= 0.75 C_{pack}\rho_{hBN} = 0.6\rho_{hBN}.\end{aligned} \tag{37}$$

Knowing the density of a crystalline hBN to be $\rho_{hBN} = 2.3$ g/cm^3, Eq. (37) gives $\rho_{fiber} = 1.38$ g/cm^3.

4.3. Piezoelectric properties of a BNNT fiber

The direct piezoelectric coefficient per unit volume for a BNNT fiber with a given distribution $n_L(R)$, from Eq. (28) is calculated as

$$e_{11,fiber} = \frac{\sqrt{N_{fiber}}}{S_{fiber}H}\left(\sum_{L=1,3}\int_0^\infty e_{11,L}^{odd}(R) n_L(R) dR + \sum_{L=2,4}\int_0^\infty e_{11,L}^{even}(R) n_L(R) dR\right) \tag{38}$$

with $e_{11,L}^{even}$ and $e_{11,L}^{odd}$ given by Eqs. (22a) and (22b), respectively. The $\sqrt{N_{fiber}}$ multiplier accounts for the random choice between positive and negative alignment of individual nanotubes along the axis of the fiber. The "odd"-integral term in Eq. (38) is similar to the integral in (30a) and gives

$$\int_0^\infty e_{11,L}^{odd}(R) n_L(R) dR = n_{0,L}\frac{H}{\Delta R} e_{11}\pi^{3/2}\sigma_L[2\bar{R}_L - (L-1)h]. \tag{39a}$$

Noting that $e_{11,L}^{even} = -\pi L h e_{11} H$ does not depend on R, the "even"-integral term in Eq. (38) gives

$$\int_0^\infty e_{11,L}^{even}(R) n_L(R) dR = -n_{0,L}\frac{H}{\Delta R} e_{11}\pi^{3/2}\sigma_L hL. \tag{39b}$$

After performing the integration, Eq. (38) takes the form

$$e_{11,fiber} = \frac{\sqrt{N_{fiber}}}{S_{fiber}}\frac{1}{\Delta R} e_{11}\pi^{3/2}\left\{\sum_{L=1,3} n_{0,L}\sigma_L[2\bar{R}_L - (L-1)h] - \sum_{L=2,4} n_{0,L}\sigma_L hL\right\}. \tag{40}$$

After expressing S_{fiber} from Eq. (32) and using Eq. (32a,b)

[2] The packing value may be highly overestimated, because there are some indications that BNNTs avoid dense packing in conglomerates.

$$e_{11,fiber} = \frac{C_{pack}e_{11}}{\sqrt{N_{fiber}}} \frac{\sum_{L=1,3} n_{0,L}\sigma_L[2\bar{R}_L - (L-1)h] - \sum_{L=2,4} n_{0,L}\sigma_L hL}{\sum_{L=1}^{4} n_{0,L}\sigma_L(\frac{1}{2}\sigma_L^2 + \bar{R}_L^2)}$$
$$= \frac{C_{pack}e_{11}}{\sqrt{N_{fiber}}} 0.686 \text{ e/nm}^2. \quad (41)$$

Using the value for $e_{11} = 2.14$ e/nm $= 3.42 \times 10^{-10}$ C/m, calculated from Eq. (18), $N_{fiber} = 1000$, and $C_{pack} = 0.8$, then $e_{11,fiber} = 0.037$ e/nm^2 $= 0.0059$ C/m^2. Compared to the piezoelectric coefficient of a hypothetical hBN crystalline material, calculated [4] as $e_{3D} = 0.76$ C/m^2, the result for a BNNT fiber is much lower. This weak piezoelectric behavior of a fiber is mostly due to two factors: (i) the assumed random alignment of the individual nanotubes, introducing the $\frac{1}{\sqrt{N_{fiber}}}$ coefficient, and (ii) the AA' stacking of the nanotube wall layers, leading to a partial cancellation of the polarization of each layer.

The converse piezoelectric coefficient for the considered BNNT fiber defined as

$$d_{11,fiber} = \frac{e_{11,fiber}}{Y_{fiber}}, \quad (42)$$

After using the already calculated values for $e_{11,fiber} = 0.0059$ C/m^2, and $Y_{fiber} = 0.410$ TPa, Eq. (42) gives $d_{11,fiber} = 0.0144$ pm/V. Both results for $e_{11,fiber}$, and $d_{11,fiber}$, show that unless the individual tube orientation is controlled, the piezoelectric properties of a BNNT fiber are rather weak and decreasing proportionally with increasing the fiber thickness (assuming that the fiber thickness is proportional to $\sqrt{N_{fiber}}$).

5. Conclusion

This study applied the previously developed SW-BNNT piezoelectric molecular dynamics model [21] to study the stiffness and piezoelectric properties of MW-BNNTs that are more commonly synthesized. The interlayer interactions in the MW-BNNTs were represented by an improved Lennard-Jones type of potential, fitted to closely reproduce the van der Waals forces as calculated from first principles calculations [29,30]. Nanotubes of the zig-zag (m, 0)-type made of one to ten layered walls were simulated in equilibrium, and under uniaxial tension to examine their elastic and piezoelectric properties. Analytical relations were derived to support the simulations and make predictions for a hypothetical BNNT fiber consisting of 1000 nanotubes that match the experimentally obtained diameter and wall number distribution. The results can be summarized as follows.

The potential energy of MW-BNNTs in equilibrium shows the existence of crossover radii where the number of wall layers is expected to change (Fig. 4). This finding enables the prediction of the possible range of radii for MW-BNNTs of a given number of walls. The prediction for BNNTs of one to four walls are found to overlap with the lower end of experimentally reported ranges [42], and slightly underestimates the expected nanotube thickness.

MW-BNNTs are predicted to experience a significant spontaneous polarization in equilibrium state. The spontaneous polarization is a result of the tube wall curvature [21], but also ascribed to the internal incompatibility strain experienced by the layers due to their discrete atomic structure. The simulations indicate that this spontaneous polarization is strongest for BNNTs of radii between 2 and 3 nm and is likely to diminish at larger radii (Fig. 8).

The elastic properties of MW-BNNTs generally follow the expectation of the shell model for BNNTs, developed by Song et al. [33]. The van der Waals forces, acting between the BNNT layers play the role of slightly decreasing the Young's modulus.

The piezoelectric properties of MW-BNNTs show significant differences for nanotubes of even vs. odd number of layers. The reason is in the alternating polarization direction in the adjacent hBN layers with AA' stacking sequence. As a result (Fig. 11), the direct tensile polarization coefficient e_{11} for odd-layer BNNTs *increases* with an increase of the tube radius R, and *decreases* with an increase of the number of layers L. By contrast, e_{11} of even-layer BNNTs remains *constant* with R, but *increases* with L. Analytically, these relations are expressed through Eqs. (22a) and (22b). The converse piezoelectric coefficient $d_{11} \sim e_{11}/Y$ also has different behavior for odd- versus even-layer BNNTs (Fig. 12). In the case of even-layer BNNTs, d_{11} *decreases* with R as $1/R$, but remains mostly *independent* of L when $R \gg Lh$ (hollow nanotubes) Eq. (26a). In the case of odd-layer BNNTs, d_{11} *scales* as $1/Lh$ *independent* of R, Eq. (26b). For full nanotubes of both types, i.e., BNNTs for which $R \to Lh$, d_{11} scales as $1/R$, Eq. (27).

The derived analytical expressions for the elastic and piezoelectric properties of an isolated BNNT are used to predict the physical properties of an example system, representing a BNNT fiber composed of 1000 BNNTs having an experimentally established diameter and wall number distribution. The calculated Young's modulus of the fiber is found to be about 55% of the theoretical Young's modulus for an hBN sheet, while the mass density of the fiber is about 60% that of a crystalline hBN, or 1.38 g/cm^3.

The calculations show that the piezoelectric properties of a BNNT fiber are rather weak and decreasing proportionally with increasing the fiber thickness. This weak piezoelectric behavior is mostly due to two factors: (i) the assumed random sense of polarization of the individual nanotubes in the fiber direction, and (ii) the AA' stacking of the nanotube wall layers, leading to a partial cancellation of the polarization of each layer. A possible way to increase the piezoelectric response of the fiber could be to control the orientation of individual nanotubes to be predominantly in one direction, rather than being random.

Acknowledgments

V. Yamakov is sponsored through cooperative agreement NNL09AA00A with the National Institute of Aerospace. C. Park and C. Ke acknowledge that their work was funded in part by the US Air Force Office of Scientific Research - Low Density Materials program under Grant Nos. FA9550-11-1-0042 and FA9550-15-1-0491. The authors appreciate the support of the NASA Langley Research Center Internal Research and Development program.

Appendix A

Performing the integration in Eqs. (30a), (33a), (35), (38), and (39) leads to solving the following series of integrals:

$$I_0 = \int_0^\infty \exp\left[-\frac{(R-\bar{R}_L)^2}{\sigma_L^2}\right] dR, \quad (A1)$$

$$I_1 = \int_0^\infty R \exp\left[-\frac{(R-\bar{R}_L)^2}{\sigma_L^2}\right] dR, \quad (A2)$$

and

$$I_2 = \int_0^\infty R^2 \exp\left[-\frac{(R-\bar{R}_L)^2}{\sigma_L^2}\right] dR. \quad (A3)$$

Applying the substitution $x = \frac{R-\bar{R}_L}{\sigma_L}$, and using

$$\int_a^\infty \exp(-x^2)dx = \frac{\sqrt{\pi}}{2}[1 - erf(a)], \quad (A4)$$

$$\int_a^{\infty} x\exp(-x^2)dx = \frac{1}{2}\exp(-a^2), \tag{A5}$$

and

$$\int x^2\exp(-x^2)dx = \frac{1}{4}\sqrt{\pi}erf(x) - \frac{x}{2}\exp(-x^2), \tag{A6}$$

where $erf(x) = \frac{2}{\sqrt{\pi}}\int_0^x \exp(-t^2)dt$, one gets, respectively:

$$I_0 = \sigma_L\frac{\sqrt{\pi}}{2}\left[1 + erf\left(\frac{\bar{R}_L}{\sigma_L}\right)\right] \underset{\bar{R}_L/\sigma_L \gg 1}{\rightarrow} \sigma_L\sqrt{\pi}, \tag{A7}$$

$$I_1 = \frac{1}{2}\sigma_L^2\exp\left[-\left(\frac{\bar{R}_L}{\sigma_L}\right)^2\right] + \sigma_L\bar{R}_L \times \frac{\sqrt{\pi}}{2}\left[1 + erf\left(\frac{\bar{R}_L}{\sigma_L}\right)\right] \underset{\bar{R}_L/\sigma_L \gg 1}{\rightarrow} \sigma_L\bar{R}_L\sqrt{\pi}, \tag{A8}$$

and

$$I_2 = \frac{1}{2}\sigma_L\left\{\sigma_L\bar{R}_L\exp\left[-\left(\frac{\bar{R}_L}{\sigma_L}\right)^2\right] + \sqrt{\pi\left(\frac{1}{2}\sigma_L^2 + \bar{R}_L^2\right)}\left[1 + erf\left(\frac{\bar{R}_L}{\sigma_L}\right)\right]\right\} \underset{\bar{R}_L/\sigma_L \gg 1}{\rightarrow} \sigma_L\sqrt{\pi}\left(\frac{1}{2}\sigma_L^2 + \bar{R}_L^2\right). \tag{A9}$$

All integrals in Section 4 can be presented as linear combinations of I_0, I_1, and I_2. For the values for $\bar{R}_L$, and σ_L, provided in Table 5, the ratio $\bar{R}_L/\sigma_L > 2.4$, gives less than 0.1% error in the limiting values of the right side of Eqs. (A7)–(A9), which justifies the used approximation when solving the integrals in Section 4.

References

[1] D. Golberg, Y. Bando, C. Tang, C. Zhi, Adv. Mater. 19 (2007) 2413.
[2] M.L. Cohen, A. Zettl, Phys. Today 63 (2010) 34.
[3] E.J. Mele, P. Král, Phys. Rev. Lett. 88 (2002) 056803.
[4] N. Sai, E.J. Mele, Phys. Rev. B 68 (2003) 241405.
[5] S.M. Nakhmanson, A. Calzolari, V. Meunier, J. Bernholc, M.B. Nardelli, Phys. Rev. B 67 (2003) 235406.
[6] H.J. Xiang, Z.Y. Chen, J.L. Yang, J. Comp. Theor. Nanosci. 3 (2006) 838.
[7] N.G. Lebedev, L.A. Chernozatonskii, Phys. Solid State 48 (2006) 2028.
[8] J.H. Kang, G. Sauti, C. Park, V.I. Yamakov, K.E. Wise, S.E. Lowther, C.C. Fay, S.A. Thibeault, R.G. Bryant, ACS Nano 9 (2015) 11942.
[9] F. Ahmadpoor, P. Sharma, Nanoscale 7 (2015) 16555.
[10] X. Wei, M.-S. Wang, Y. Bando, D. Golberg, Adv. Mater. 22 (2010) 4895.
[11] N.G. Chopra, A. Zettl, Solid State Commun. 105 (1998) 297.
[12] R. Arenal, M.-S. Wang, Z. Xu, A. Loiseau, D. Golberg, Nanotechnology 22 (2011) 265704.
[13] E. Hernandez, C. Goze, P. Bernier, A. Rubio, Phys. Rev. Lett. 80 (1998) 4502.
[14] H.M. Ghassemi, C.H. Lee, Y.K. Yap, R.S. Yassar, J. Appl. Phys. 108 (2010) 024314.
[15] D.-M. Tang, C.-L. Ren, X. Wei, M.-S. Wang, C. Liu, Y. Bando, D. Golberg, ACS Nano 5 (2011) 7362.
[16] A.P. Suryavanshi, M.-F. Yu, J. Wen, C. Tang, Y. Bando, Appl. Phys. Lett. 84 (2004) 2527.
[17] D. Golberg, P.M.F.J. Costa, O. Lourie, M. Mitome, X. Bai, K. Kurashima, C. Zhi, C. Tang, Y. Bando, Nano Lett. 7 (2007) 2146.
[18] Y. Zhao, X. Chen, C. Park, C.C. Fay, S. Stupkiewicz, C. Ke, J. Appl. Phys. 115 (2014) 164305.
[19] M. Zheng, X. Chen, C. Park, C.C. Fay, N.M. Pugno, C. Ke, Nanotechnology 24 (2013) 505719.
[20] S. Thibeault, J.H. Kang, G. Sauti, C. Park, C. Fay, G. King, MRS Bull. 48 (2015) 836.
[21] V. Yamakov, C. Park, J.H. Kang, K.E. Wise, C. Fay, Comp. Mater. Sci. 95 (2014) 362.
[22] J. Tao, G. Xu, Y. Sun, Math. Probl. Eng. 2015 (2015) 240547.
[23] R. Ansari, S. Ajori, Phys. Lett. A 378 (2014) 2876.
[24] S. Ajori, R. Ansari, Curr. Appl. Phys. 14 (2014) 1072.
[25] M.W. Smith, K.C. Jordan, C. Park, J.-W. Kim, P.T. Lillehei, R. Crooks, J.S. Harrison, Nanotechnology 20 (2009) 505604.
[26] R. Ansari, S. Ajori, Appl. Phys. A 120 (2015) 1399.
[27] R. Ansari, S. Ajori, Superelasticity Microstruct. 93 (2016) 18.
[28] R. Ansari, S. Ajori, A. Ameri, Appl. Surf. Sci. 366 (2016) 233.
[29] N. Marom, J. Bernstein, J. Garel, A. Tkatchenko, E. Joselevich, L. Kronik, O. Hod, Phys. Rev. Lett. 105 (2010) 046801.
[30] O. Hod, J. Chem. Theory Comput. 8 (2012) 1360.
[31] J. Zhang, S.A. Meguid, J. Phys. D: Appl. Phys. 48 (2015) 495301.
[32] M.S. Dresselhaus, G. Dresselhaus, P.C. Eklund, Science of Fullerences and Carbon Nanotubes, Academic, San Diego, 1996.
[33] J. Song, J. Wu, Y. Huang, K.C. Hwang, H. Jiang, J. Nanosci. Nanotechnol. 8 (2008) 3774.
[34] A.L. Tiano, C. Park, J.W. Lee, H.H. Luong, L.J. Gibbons, S.-H. Chu, S. Applin, P. Gnoffo, S. Lowther, H.J. Kim, et al., Proc. SPIE-Int. Soc. Opt. Eng. 9060 (2014) 906006.
[35] C. Sevik, A. Kinaci, J.B. Haskins, T. Cagin, Phys. Rev. B 84 (2011) 085409.
[36] S.K. Singh, M. Neek-Amal, S. Costamagna, F.M. Peeters, Phys. Rev. B 87 (2013) 184106.
[37] K. Albe, W. Möller, K.-H. Heinig, Radiat. Eff. Defects Solids 141 (1997) 85.
[38] W. Sekkal, B. Bouhafs, H. Aourag, M. Certier, J. Phys. Cond. Matter 10 (1998) 4975.
[39] J.H. Warner, M.H. Rümmeli, A. Bachmatiuk, B. Büchner, ACS Nano 4 (2010) 1299.
[40] K.N. Kudin, G.E. Scuseria, B.I. Yakobson, Phys. Rev. B 64 (2001) 235406.
[41] Q. Peng, W. Ji, S. De, Comp. Mater. Sci. 56 (2012) 11.
[42] M. Zheng, C. Ke, I.-T. Bae, C. Park, M.W. Smith, K. Jordan, Nanotechnology 23 (2012) 095703.
[43] M. Zheng, X. Chen, I.-T. Bae, C. Ke, C. Park, M.W. Smith, K. Jordan, SMALL 8 (2012) 116.
[44] M. Zheng, L.-F. Zou, H. Wang, C. Park, C. Ke, ACS Nano 6 (2012) 1814.
[45] M. Zheng, L. Zou, H. Wang, C. Park, C. Ke, J. Appl. Phys. 112 (2012) 104318.
[46] K.-A.N. Duerloo, M.T. Ong, E.J. Reed, J. Phys. Chem. Lett. 3 (2012) 2871.